Petroleum Science 20 (2023) 3251–3263

Contents lists available at ScienceDirect

Petroleum Science

journal homepage: www.keaipublishing.com/en/journals/petroleum-science

Original Paper

Developing single-atom catalyst-based epoxy coating with active nanocatalytic anticorrosion performance in oxygen environment

Meng Cheng [a], Yu-Qi Liu [a], Hao Jiang [a], Jun-Hao Liu [a], Chun-Ling Li [a, b], Shuang-Qing Sun [a, b, **], Song-Qing Hu [a, b, *]

[a] School of Materials Science and Engineering, China University of Petroleum (East China), Qingdao, 266580, Shandong, China
[b] Institute of Advanced Materials, China University of Petroleum (East China), Qingdao, 266580, Shandong, China

ARTICLE INFO

Article history:
Received 14 September 2022
Received in revised form
12 December 2022
Accepted 26 May 2023
Available online 27 May 2023

Edited by Jia-Jia Fei

Keywords:
Nanocatalytic anticorrosion
Pre-constrained metal ions
Single-atom Fe–N–C
Deoxygenation agent
Smart coatings

ABSTRACT

The stimuli-responsive anticorrosion coatings have drawn great attention as a prospective corrosion protection approach due to their smart self-repairing properties. In contrast to passive protection mechanism based on post-corrosion microenvironmental changes, a unique active protection strategy based on nanocatalytic oxygen depletion is proposed in this work to inhibit the occurrence of corrosion. Porous Fe–N–C catalysts with outstanding oxygen reduction reaction (ORR) activity (half-wave potential of 0.89 V) is firstly synthesized through pre-coordination with organosilane precursor to obtain homogeneously distributed active sites. When this catalyst is introduced into the coating matrix, uniformly distributed Fe–N–C not only compensates the defects but plays a crucial role in adsorption and consumption of diffused oxygen in the coating. Under this dual action, the penetration of corrosive medium, especially oxygen, through coating to metal substrate is greatly suppressed, resulting in effective corrosion inhibition and a significant increase in corrosion resistance of the composite coating compared to pure epoxy coating. This work provides a new perspective and the starting point for the design of high-performance smart coating with active anticorrosion properties.

1. Introduction

From offshore equipment to oil-gas wells and pipelines, metal materials have become the muscles and bones of modern society due to their excellent mechanical properties, wide variety of sources and low cost (Bahremand et al., 2021; Machuca et al., 2014; Suedile et al., 2014). Nevertheless, the inevitable metal corrosion during service remains a major concern in applications with great economic losses and many security issues (Borisova et al., 2012; Zhao et al., 2016). Considerable efforts have been made to address this much-vexed problem (He et al., 2018; Yu et al., 2015). Among numerous corrosion protection methods, organic coatings and corrosion inhibitors are two of the most potent ways to mitigate or prevent the steel corrosion (Qiu et al., 2017; Ye et al., 2018; Liu et al., 2018; Abdullayev et al., 2013). Unfortunately, the physical barrier function of organic coatings gradually loses and fails with time in service. This is because the inherent pores and cracks in organic coatings serve as diffusion path for corrosive species (H_2O, O_2, Cl^-) and the constant permeation will lead to the coating detachment from metal substrate and finally aggravate corrosion (Sun et al., 2015; Mao et al., 2015; Liu et al., 2018). In this context, the combination of corrosion inhibitors and organic coatings becomes a promising strategy for enhancing corrosion protection.

At the outset of the study, inhibitors were directly incorporated into organic coatings without obtaining the desired corrosion protection properties. As reported, direct contact of the corrosion inhibitor with the coating matrix can lead to compromised coating integrity (Qian et al., 2017; Borisova et al., 2011). Moreover, randomly dispersed corrosion inhibitors may escape from the coating, causing coating defects and providing channels for the penetration of corrosive media (Zheludkevich et al., 2007; Borisova et al., 2013; Tavandashti et al., 2016). Therefore, the rational doping pattern of inhibitors and the ability to repair defective area are two

* Corresponding author. School of Materials Science and Engineering, China University of Petroleum (East China), Qingdao, 266580, Shandong, China.
** Corresponding author. School of Materials Science and Engineering, China University of Petroleum (East China), Qingdao, 266580, Shandong, China.
E-mail addresses: sunshuangqing@upc.edu.cn (S.-Q. Sun), songqinghu@upc.edu.cn (S.-Q. Hu).

https://doi.org/10.1016/j.petsci.2023.05.019

key factors to improve anticorrosion performance. Since the concept of smart coating was pioneered by White et al. (2001), substantial efforts have been paid on realizing the self-healing ability of anticorrosion coatings (Shchukin and Möhwald, 2007; Qian et al., 2019; Zheng et al., 2013; Zhao et al., 2020; Liu et al., 2021; Najmi et al., 2021). Researches have found that introducing the encapsulated inhibitors by nanocontainers into coatings will avoid the directly contact between inhibitors and coating matrix and ensure the coating integrity. Most notably, the introduced nanocontainers are sensitive to the microenvironment change at corrosion sites (e.g., pH (Fu et al., 2013; Wang et al., 2012), corrosion potential (Kim et al., 2010; Lai et al., 2013), etc.) and will release loaded inhibitors quickly to form a protective film to further restrain corrosion growth. The successful combination of the passive barrier function of organic coatings and the smart stimuli-response of active nanocontainers not only enhances anticorrosion performance, but also endows the coating with self-repairing capability. Actually, the smart function (on-demand release of inhibitors) depends on the stimuli-responsive nanovalves (e.g., polyelectrolyte shell (Skorb and Andreeva, 2013), supramolecular assembly (Li et al., 2013; Tian et al., 2016; Shen et al., 2017), etc.) installed on nanocontainers surface. Meanwhile, these gatekeepers could prevent appreciable premature leakage of inhibitors in normal environment. However, the extremely complex installation of these nanovalves would seriously limit their further development and practical application. Moreover, it's only when corrosion caused the microenvironment change, can the stimuli-responsive nanocontainers release inhibitors to complete self-repairment, so such anticorrosion is inherently passive to a certain extent, and it's hard to achieve long-term protection (Ye et al., 2020). As the saying goes “prevention is better than cure”. How to proactively prevent corrosion before it occurs is a more effective strategy and a higher challenge for designing advanced smart anticorrosion coatings.

Metals are prone to corrosion in humid air, especially under high pressure air injection conditions that are applied to enhance oil production, with oxygen as depolarizing agent participating corrosion process (Tian et al., 2019; Sun et al., 2022; Wang et al., 2022; Ning et al., 2021; Zeng et al., 2021). However, the aforementioned stimuli-responsive coatings offer little corrosion protection to metals serving in harsh oxygen environments. Given the fact that organic coatings work by blocking the corrosive medium from the metal substrate, it is expected that the reduction of oxygen content in the coating can be effective in inhibiting corrosion to some extent. On this basis, introducing additional catalytic functions to spontaneously eliminate corrosive species (e.g., O_2) while improving the impermeability of organic coatings would greatly improve their corrosion resistance. Such coating performance enhancement realized by catalyst in harsh environment is defined as active nanocatalytic anticorrosion. Inspired by oxygen reduction reaction (ORR) studies, if catalyst is introduced into organic coatings, the diffused O_2 in coating could be reduced to H_2O_2 or H_2O, which will reduce the contribution of O_2 to corrosion process. However, the generated H_2O_2 through two-electron process will destroy the coating stability due to its strong oxidizing effect. Therefore, the search for more efficient ORR catalyst (reduction product is only H_2O) is crucial for the design of new anticorrosion coatings. Recently, single-atom catalysts (SACs) have been found to exhibit ideal four-electron catalytic pathway with excellent electrochemical activity and cycling stability, making them the most promising catalysts to replace noble metals (Jin et al., 2021; Luo et al., 2021; Zhou et al., 2020). Among them, the Fe—N—C catalysts have received the most extensive attention due to their easy-to-design active centers and low cost. At present, SACs are usually obtained by direct pyrolysis of precursors. Such high-temperature treatment often leads to the aggregation of metal atoms, which is detrimental to the catalytic performance. For example, zeolitic imidazolate frameworks (ZIFs) constructed from tetrahedral transition metals and imidazolate ligand are widely used as ideal precursors to prepare electrocatalysts with atomically dispersed metal sites. However, single and evenly distributed active sites without agglomeration in target electrocatalysts cannot be obtained by direct calcination of ZIFs. To address this issue, confined strategies such as silica shell protected pyrolysis was developed to obtain catalysts with higher concentration of dispersed active sites, where the structure can be well controlled, but the monodisperse state of metal atoms cannot be precisely controlled by this physical nanoconfinement effect (Li et al., 2020; Qu et al., 2019). Therefore, there is an urgent need to develop optimal preparation methods to boost the ORR activity and durability of the SACs. On this foundation, together with the required coating compatibility, embedded catalysts as reactive deoxygenation agent are expected to significantly improve the protective effects of anticorrosion coatings.

In this work, a “pre-coordination” strategy that utilizes the coordination behavior of organosilane precursors and metal ions to achieve the molecular anchoring effect is firstly proposed to construct single-atom Fe—N—C catalysts. The isolated Fe—N—C moiety is chemically anchored in the organosilica framework and the atomically dispersed Fe—N active sites are precisely gained without agglomeration, showing desired oxygen reduction performance. Then, a novel active protection strategy based on nanocatalytic oxygen depletion is proposed and applied for the first time to smart anticorrosion coatings. By introducing the highly efficient and stable Fe—N—C catalyst, the prepared composite coating exhibits significantly improved anticorrosion performance. Specifically, the uniformly dispersed Fe—N—C catalysts not only boost barrier properties of the coating but serve as smart control unit to automatically reduce O_2 content to prevent corrosion. To sum up, this active nanocatalytic anticorrosion coating exhibits unique proactive protection performance and innovative long-acting mechanism, which will provide new experience and reference for the construction of smart anticorrosion coating with great application potential.

2. Materials and methods

Materials: Cetyltrimethylammonium bromide (CTAB, 99%, Aladdin), 1,10-Phenanthrolin-5-amine (97%, Aladdin), 3-Chloropropyltriethoxysilane (98%, Aladdin), $FeSO_4·7H_2O$ (99%, Aladdin). $Zn(NO_3)_2·6H_2O$ (AR), tetraethyl orthosilicate (TEOS, AR), N,N-Dimethylformamide (DMF, AR), methanol (AR), ethanol (AR), sodium hydroxide (NaOH, AR) and hydrogen fluoride (HF, AR) were purchased from Sinopharm. Deionized (DI) water was used in all experiments.

Synthesis of Phen precursor: 0.27 mL 3-chloropropyltriethoxysilane was added into DMF solution of 0.2 g 1,10-phenanthrolin-5-amine, which was then allowed to react at 70 °C under N_2 for 72 h. The generated hydrochloric acid in the reaction was neutralized through addition of triethylamine. After vacuum removal of reagent, washed with ethanol and hexane, reddish brown product was obtained.

Synthesis of Fe-Phen organosilica: Firstly, 11.12 mg $FeSO_4·7H_2O$ and 91 mg **Phen** precursor were mixed in ethanol to prepare pre-coordination complex. Then, the complex was added into 60 mL aqueous solution containing 0.12 g CTAB and 450 μL NaOH (2 M) under 80 °C, followed by 0.5 mL TEOS. After stirring for 2 h, **Fe-Phen** organosilica was collected from cooled solution, washed with ethanol and dried. **Phen** organosilica was prepared similarly without the addition of $FeSO_4·7H_2O$.

Synthesis of Fe—N—C: Fe-Phen organosilica was placed in tubular furnace and pyrolyzed at 900 °C for 3 h under N_2 flow with

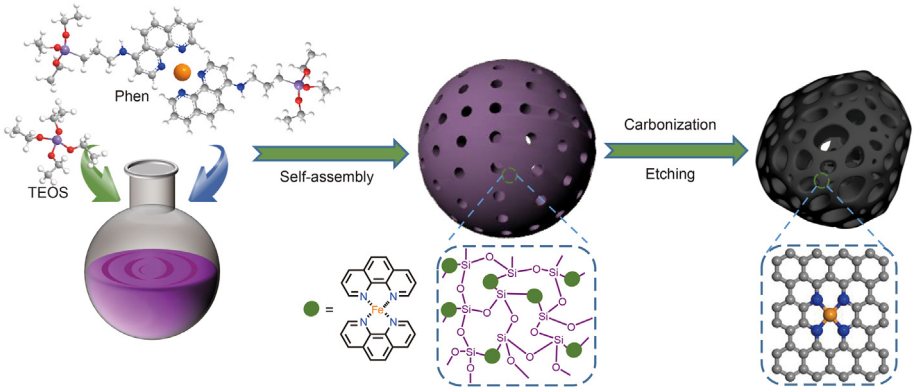

Scheme 1. Preparation process of Fe–N–C catalyst.

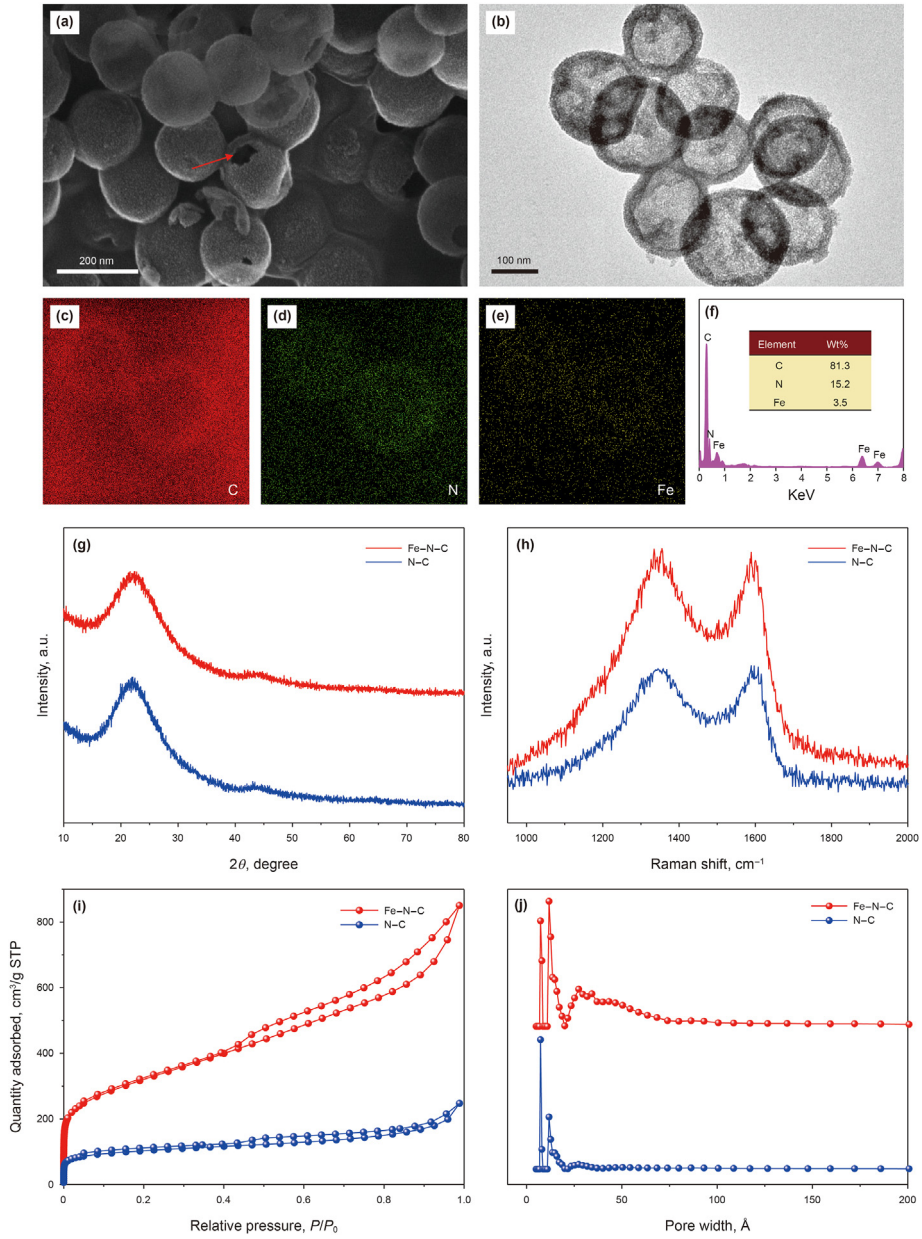

Fig. 1. (**a**) SEM image, (**b**) TEM image, (**c**–**f**) element mappings and contents of Fe–N–C. (**g**) XRD patterns, (**h**) Raman spectra, (**i**) N_2 adsorption-desorption isotherm and (**j**) pore size distribution of Fe–N–C and N–C.

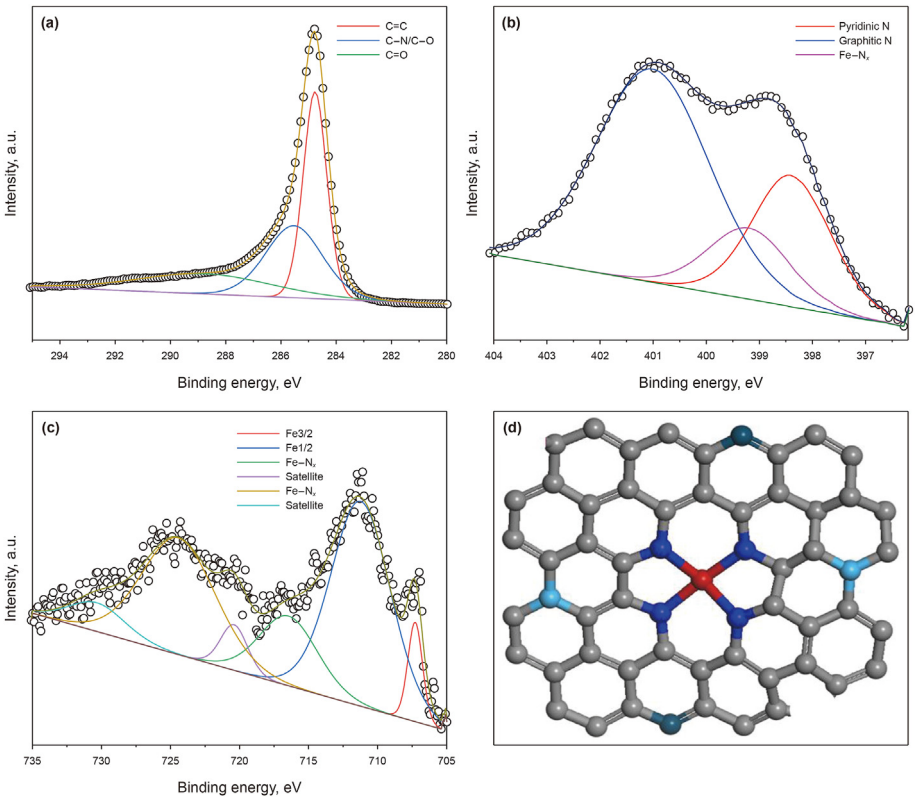

Fig. 2. (**a**) C 1s, (**b**) N 1s, (**c**) Fe 2p XPS spectrum of Fe–N–C and (**d**) the N species in carbon framework.

heating rate of 5 °C min^{-1}. Obtained powder was etched by 10% HF solution to afford Fe–N–C catalysts. The N–C was prepared by pyrolysis of **Phen** organosilica under the same condition.

Preparation of active anticorrosion coating: Fe–N–C catalyst (0, 0.5, 1, 3 g L^{-1}) was well mixed with epoxy to form homogeneous mixture, which was subsequently deposited on mind steel by automatic coater. Pure epoxy coating was synthesized by the same method in absence of Fe–N–C. The coating named EP-*n* (*n* denotes Fe–N–C amount). For comparison, coating with N–C catalyst (EP-NC) was also prepared by similar method.

2.1. Characterization

The morphology of catalysts was revealed by scanning electron microscopy (SEM), and transmission electron microscopy (TEM). The phase and porous structure of catalysts were analyzed by X-ray powder diffraction (XRD) and nitrogen adsorption isotherms (BET). The X-ray photoelectron spectroscopy (XPS) and Raman analysis were performed to determine the chemical composition of Fe–N–C catalyst. The active anticorrosion performance of the coating was studied by electrochemical impedance spectroscopy (EIS) in oxygen-saturated 3.5 wt% NaCl solution. The EIS was obtained by three electrode mode in the frequency range from 10^5 to 10^{-2} Hz under a sinusoidal voltage of 10 mV. For the accuracy, the electrochemical tests were repeated three times. The corrosion products and surface morphology after test were also characterized by electron microscopy. For the oxygen permeability coefficient of coatings, the differential volume-variable pressure method is adopted according to ASTM D1434 standard under room temperature at 37% relative humidity.

3. Results and discussion

3.1. Characterization of Fe–N–C

The construction process of Fe–N–C catalyst is illustrated by Scheme 1. The molecular structure of designed **Phen** precursor was firstly confirmed by ^{1}H NMR (Fig. S1). Then, the pre-coordinated **Fe-Phen** and TEOS were assembled into organosilica framework through one-pot sol-gel process under basic condition with CTAB serving as structure directing reagent. During the synthesis process, it is difficult to control the hydrolysis and condensation of pure **Fe-Phen** organosilane and thereby the morphology of final product cannot be well regulated. The added TEOS can just act as inorganic silane to assist the growth of **Fe-Phen** precursor and realize the nanostructure control of organosilica. In addition, TEOS is prone to grow inside the nanospheres due to its faster hydrolysis and condensation, resulting in formation of solid silica/organosilica core-shell structure, as proved by electron microscopic characterization (Fig. S2(a) and (c)). More specifically, organosilica exhibits stronger hydrophobicity compared to inorganic silica due to the incorporated organic groups in the framework. Therefore, the organosilica framework is more stable than inorganic silica against attacking of aqueous solution. Based on this difference in chemical stability, the inner region of solid nanospheres is selectively etched when incubated in water, while the organosilica is well preserved and hollow spheres emerged (Fig. S2(b) and (d)). The target Fe–N–C catalyst will be obtained via carbonization under inert atmosphere and subsequent HF etching. In addition, N–C catalyst was prepared by similar synthetic route without Fe addition.

The micromorphology and structure of Fe–N–C catalyst are displayed in SEM and TEM images of Fig. 1(a) and (b). The obtained

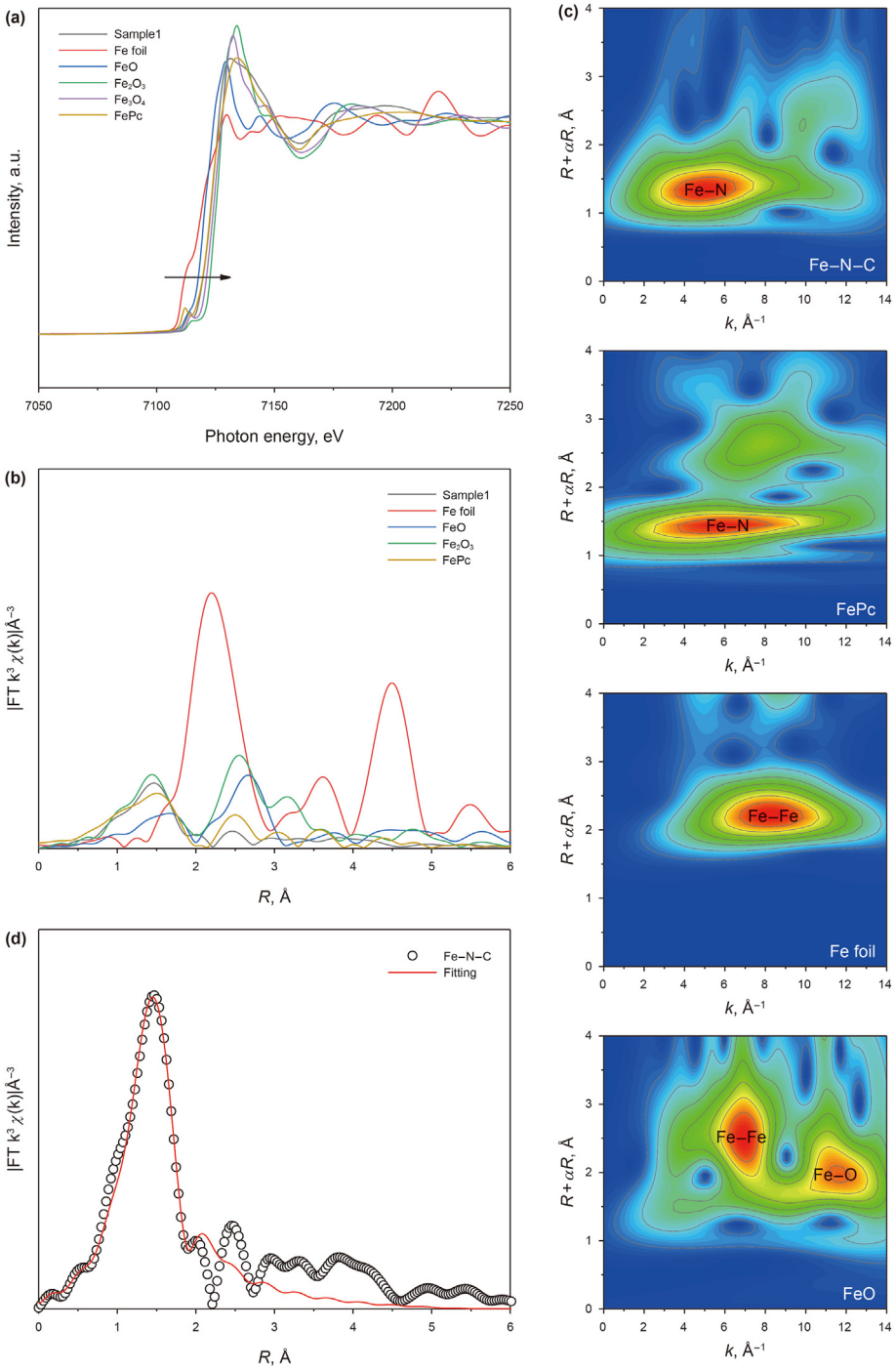

Fig. 3. (**a**) Fe K-edge XANES spectra, (**b**) Fourier transformed magnitudes, (**c**) wavelet transform contour map of Fe–N–C and the references, (**d**) R-space EXAFS fitting curve of Fe–N–C.

Fe–N–C presents a uniform spherical morphology, and the rupture of shell (red arrow) suggests the existence of hollow core. The TEM image in Fig. 1(b) further demonstrates that the designed Fe–N–C catalyst possesses hollow structure with homogenous element distribution (C, N, Fe in Fig. 1(c)–(f)). Then, XRD patterns are emphasized to characterize the graphitization degree of Fe–N–C catalyst. In the XRD of Fe–N–C (Fig. 1(g)), two characteristic peaks appear at 24° and 44°, which are indexed to the (002) and (101) planes and could prove the existence of graphitic carbon. N–C exhibits similar phase structure, implying the absence of metal atom aggregation in Fe–N–C catalyst. Moreover, the defect degree of Fe–N–C catalyst is investigated by Raman spectra. It can be found that there is considerable defect structure in Fe–N–C catalyst, which is manifested by the emergency of D band at 1330 cm^{-1} and higher I_D/I_G indicator of 1.02 compared to relatively lower I_D/I_G of N–C (0.96). This is the direct and compelling evidence for the defect structure induced by effective doping of Fe single atom in Fe–N–C catalyst. Then, the porous structure of Fe–N–C catalyst is demonstrated by N_2 adsorption-desorption measurements. A typical IV isotherm with a H3-type hysteresis loop is observed in

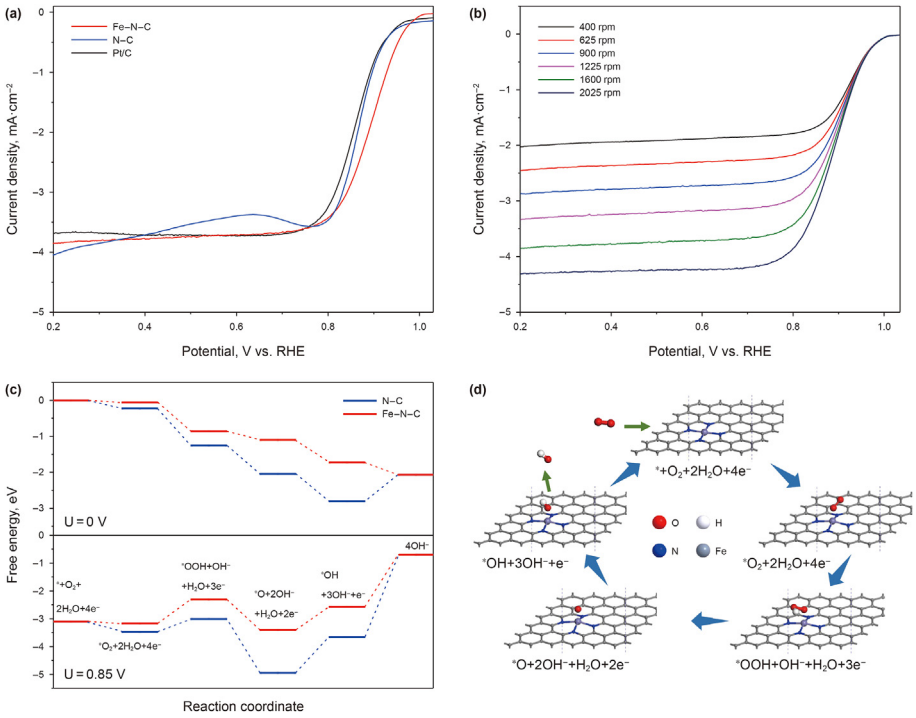

Fig. 4. (**a**) LSV curves of Fe–N–C and N–C in oxygen-saturated 0.1 M KOH solution under 1600 rpm, (**b**) LSV curves of Fe–N–C under different rotating speeds from 400 to 2025 rpm, (**c**) Free energy gradient on Fe–N–C and N–C for the ORR (U = 0 and 0.85 V), (**d**) proposed ORR pathway on Fe–N–C.

Fig. 1(i), expressing the mesopore-dominated pore structure of Fe–N–C. According to the pore size distribution in Fig. 1(j), the pores of Fe–N–C are concentrated at 1.18 and 2.73 nm. In spite of similar porous structure of N–C, Fe–N–C possesses a higher specific surface area of 1110.6 $m^2\ g^{-1}$ and a larger total pore volume of 1.23 $cm^3\ g^{-1}$. As reported, the higher specific surface area of catalyst can expand the contact with reaction media and the mesopores are beneficial for the mass transfer, thereby exhibiting superior oxygen reduction activity.

XPS is performed to further explore the element composition and binding state of the Fe–N–C catalyst. Three distinct peaks appear in the full-scale survey, demonstrating the existence of Fe, N and C element (Fig. S4). Next, the high-resolution XPS spectra of C 1s, N 1s and Fe 2p are further deconvoluted. Fig. 2(a) shows three C characteristics at 284.8 (C=C), 285.5 (C–N/C–O) and 289.0 eV (C=O). The appearance of C–N bonds successfully confirms the doping of N into carbon framework. Meanwhile, the high-resolution spectrum of N 1s is fitted into three peaks at 398 (pyridinic N), 399.5 (Fe–N) and 401.2 eV (graphitic N). Defective N species, i.e., pyridinic N is reported as coordination sites for isolated Fe atom. Thanks to the pre-coordination and spatial separation effect of organosilica framework, highly efficient single-atom catalyst with considerable concentration of single-atom Fe active sites is synthesized. Moreover, the high-resolution spectrum of Fe 2p is resolved into four types of peaks in Fig. 2(c), the Fe $2p_{3/2}$ and Fe $2p_{1/2}$ peaks centered at 707.3 and 724.6 eV, the Fe–N peaks at 711.3 and 720.5 eV, and the satellite peaks at 716.7 and 730.8 eV. Based on the above, Fe atoms are mainly coordinated with N species forming Fe–N active sites, and the formed Fe–N is anchored on a conductive carbon framework with a hierarchically meso-/microporous hollow structure. The abundant active sites and unique hierarchical structure will contribute to a significant increase in the electrochemical activity of oxygen reduction.

X-ray absorption near-edge structure (XANES) and extended X-ray absorption fine structure (EXAFS) are further adopted to determine the coordination environment of the Fe single atoms in Fe–N–C. As shown of the valence states of Fe–N–C and references in the XANES spectra (Fig. 3(a), arrow indication), Fe–N–C has an absorption edge located between FeO and Fe_2O_3 and almost overlaps with iron (II) phthalocyanine (FePc), indicating that the valence of Fe in Fe–N–C is between +2 and + 3. From the R-space EXAFS spectrum of Fe–N–C, it can be found that only one peak related to Fe–N bond appears at 1.44 Å, indicating the Fe atoms are isolated. According to the EXAFS fitting results, there are four N atoms coordinating with single Fe atom and the actual bond length of Fe–N–C is about 1.93 Å, demonstrating the existence of monoatomic Fe–N_4 structure (Fig. 3(d) and Table S1). Moreover, the relatively stable plots at high-k region and identical fitting in k-space proves that no Fe–Fe bond forms in F–N–C (Fig. S5). The wavelet transform (WT) contour plots are further explored to well distinguish the coordination information of Fe–N–C (Fig. 3(c)). It can be found that there is a distinct peak in the ordinate 1.3 Å of Fe–N–C, which corresponds to the Fe–N bond. The peak location is different from that of the Fe foil and Fe_2O_3, but close to that of FePc, implying the binding state of Fe atom Fe–N rather than Fe–Fe and Fe–O bond. Up to now, the Fe–N–C catalyst with single atom Fe–N_4 active sites is considered to be successfully constructed.

3.2. Oxygen reduction property

The oxygen reduction property of Fe–N–C is identified via linear sweep voltammetry (LSV) method. Fig. 4(a) shows the LSV plot of Fe–N–C, and it can be found that Fe–N–C exhibits an onset potential (E_{onset}) of 1.02 V and a half-wave potential ($E_{1/2}$) of 0.89 V. In addition, the reference N–C without Fe doping and commercial Pt/C catalyst maintain a similar $E_{1/2}$ of 0.84 V. Based on the $E_{1/2}$ comparison, the Fe–N–C catalyst shows the most desirable ORR performance. This suggests the doped Fe atoms are atomic anchoring on organosilica framework during the hydrolysis of organosilane precursor, and this homogeneous distribution

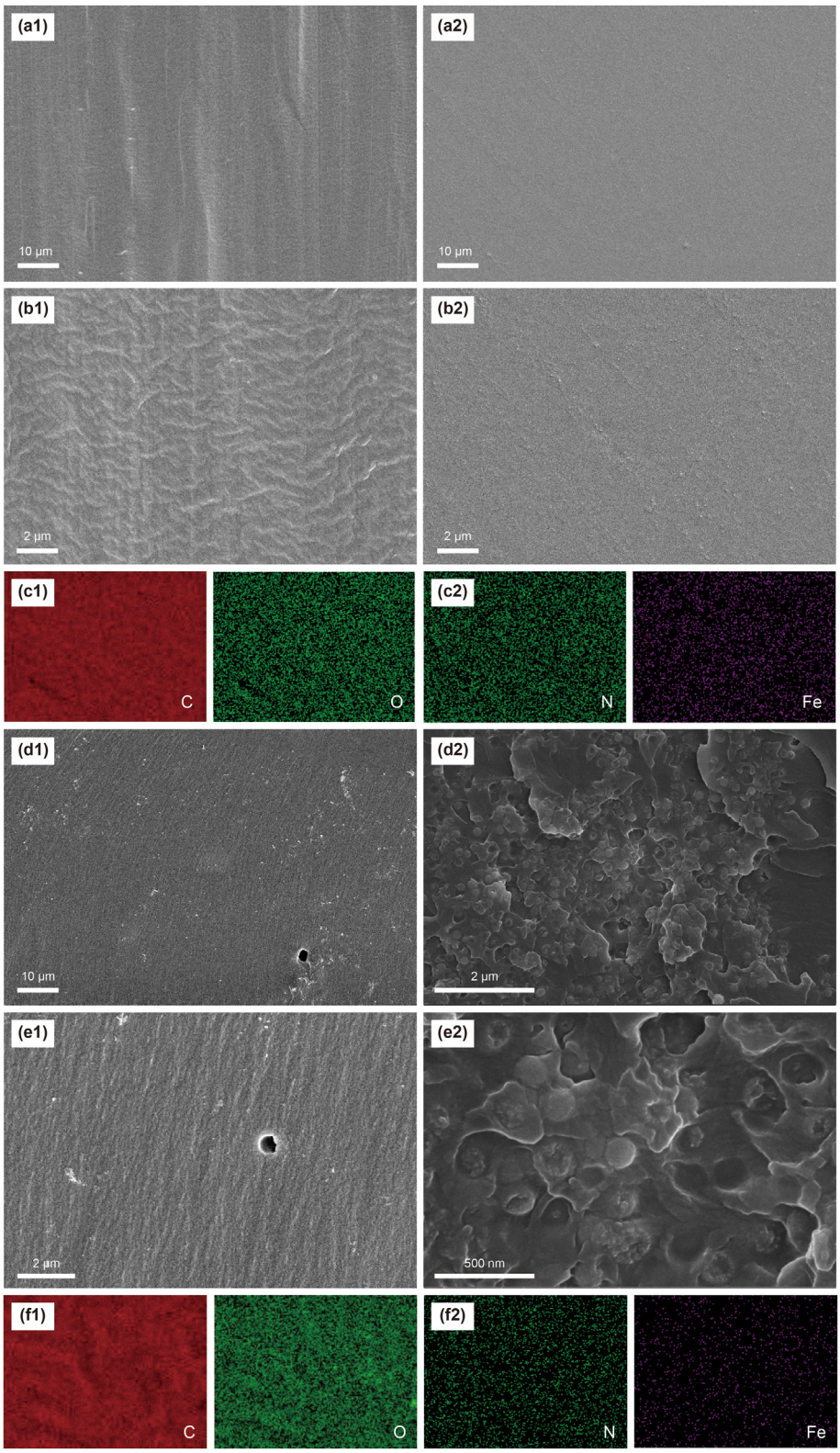

Fig. 5. SEM images and EDS mappings of (**a1**–**c1**) blank and (**a2**–**c2**) Fe–N–C doped coatings from the top view. SEM images and EDS mappings of (**d1**–**f1**) blank and (**d2**–**f2**) Fe–N–C doped coatings from the intersection view.

behavior ensures excellent ORR activity. For the deep reaction mechanism of ORR, the LSV plots under different rotation speeds are analyzed. Apparently, the limiting current density increases with the rotation speed, while the onset and half-wave potential remain unchanged. Fig. S6(a) shows the Koutecky-Levich (K-L) plots, and the curves at all potentials exhibit well-defined linearity with similar slope. This indicates that the electron transfer number (n) of Fe–N–C in ORR is almost the same. Based on the K-L

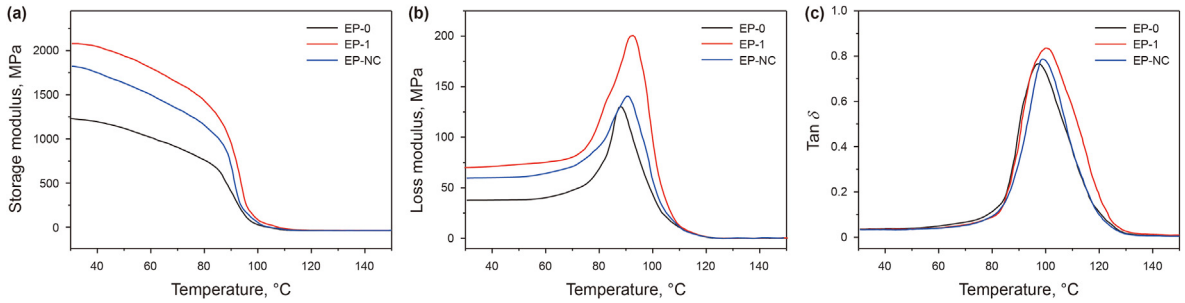

Fig. 6. DMA curves: (**a**) storage modulus, (**b**) loss modulus, and (**c**) tanδ of different coatings.

calculations, the average n of Fe–N–C is to be 3.92, which further suggests Fe–N–C prefers the four-electron path to reduce oxygen directly to water rather than hydrogen peroxide. Moreover, the Fe–N–C possess a lower tafel slope (60 mV·dec^{-1}) than Pt/C (78 mV·dec^{-1}), indicating a faster ORR kinetics (Fig. S6(d)). The long-term stability of Fe–N–C is also evaluated by chronoamperometry measurement for 30000 s under 0.5 V and cyclic CV test. It can be found that 95.4% of the initial current density is reserved and the half-wave potential only exhibits a 20 mV loss after 5000 cyclic CV compared to the initial value, which demonstrates the superior stability of Fe–N–C in ORR process. Thus, the obtained Fe–N–C catalyst can play a great role in oxygen reduction in anticorrosion coating.

To explore the potential mechanism of ORR on Fe–N–C, density functional theory (DFT) calculations are performed (see the computational detail in Supporting Information). The model of carbon supported atomic Fe–N_4 center and N-doped carbon without Fe were firstly constructed. Then, the free energy of each step in the ORR process was extracted to determine the reaction path (Fig. 4(c) and (d)). At the working potential (U = 0 V), the free energy of all the reaction steps on Fe–N–C model shows consistent decline, indicating that ORR proceeds easily at isolated Fe–N_4 sites. The reaction on N-doped carbon until generation of *OH also occurs readily, with a continuous decrease of the free energy. However, there is a thermodynamic overpotential of 0.74 eV to be overcame for the reduction of *OH to OH^- (the rate-determining step). The free energy at U = 0.85 V was also obtained, which implies that the thermodynamic overpotential during ORR processes at isolated Fe–N_4 sites is lower than that of N-doped carbon and further demonstrates that single-atom active Fe–N_4 centers are more conducive to catalyzing the oxygen reduction reaction than heterogeneous N-doped carbon. According to the experimental and simulation results, the Fe–N–C obtained by “Pre-coordination” strategy holds highly available atomic Fe–N_4 sites and provides high-efficiency in ORR process.

3.3. Active anticorrosion performance

The dispersion of Fe–N–C in epoxy coating was characterized prior to the test of anticorrosion performance. Fig. 5 shows the SEM images of pure epoxy and Fe–N–C doped coatings from the top and the intersection view. It can be found form the top-view morphology (Fig. 5(a1)–(b2)) that the introduction of Fe–N–C does not change the structure of epoxy coating, indicating that Fe–N–C does not aggregate on the surface of epoxy coating. In addition to having the same C and O elements as the pure epoxy resin (Fig. 5(c1) and Fig. S7(a)), the uniform distribution of Fe and N elements belonging to Fe–N–C in Fig. 5(c2) further demonstrates the excellent dispersion behavior of doped catalyst in the coating. From the SEM images of fracture surface, there are apparent holes in pure epoxy (Fig. 5(d1) and (e1)), which is result from the solvent volatilization during curing process. In contrast, a uniform dispersion of Fe–N–C catalyst is observed and no pores are found in the composite coating (Fig. 5(d2) and (e2). Moreover, element mappings are also obtained to vividly confirm the dispersion of Fe–N–C in the coating. Evenly distributed Fe and N elements except for the common elements (C and O) are observed, implying the well-defined dispersibility of Fe–N–C in the coating. Such morphology and elements results suggest that the introduction of Fe–N–C could disperse well and effectively limit the formation of pores during the curing process. In this case, the penetration of corrosive medium will be blocked and corrosion rate of the metal substrate will be greatly reduced. In addition, dynamic mechanical property (DMA), one of the effective methods to study the investigate the interfacial strength between filler and resin, is also provided. As shown in Fig. 6, the composite coatings exhibit higher storage modulus (EP-1: 2079.3 MPa, EP-NC: 1823.1 MPa) and more obviously increased loss modulus compared with pure epoxy (1231.8 MPa), demonstrating that the introduced nanocatalyst possesses effective interfacial interaction with resin matrix and could raise the dissipated energy resulting from specimen deformation. Based on the above morphology and DMA results, it can be concluded the introduced Fe–N–C catalyst distributes evenly in the coating matrix and has desired adhesion with resin matrix, avoiding the formation of defects and reinforcing the impermeability of the coating.

Subsequently, the corrosion resistance of coatings was evaluated by immersion experiment in oxygen-saturated 3.5 wt% NaCl solution and revealed by EIS. The Bode, Nyquist, and Phase plots of pure epoxy and Fe–N–C doped coatings are shown in Fig. 7. Obviously, the impedance modulus at 0.01 Hz ($|Z|_{0.01}$) of pure epoxy drops sharply from 2.79×10^5 to 2.16×10^4 Ω cm^2 after 30 days of immersion. In contrast, the $|Z|_{0.01}$ of the Fe–N–C doped coatings are always two orders of magnitude higher than that of EP-0, and exhibit relatively slower decline rates. Actually, $|Z|_{0.01}$ is considered as one persuasive parameter reflecting the capability of coatings to suppress the evolution of corrosion process. Generally, coatings with excellent protection performance undoubtedly have a larger impedance modulus. Accordingly, the substantial decrease in $|Z|_{0.01}$ for EP-0 implies a loss of protective property due to the penetration of corrosive medium through the coating defect, inducing the failure of the epoxy coating and corrosion of the metal substrate. The relatively high $|Z|_{0.01}$ with low decline rates of composite coatings indicates that introduced Fe–N–C with well-defined dispersion behavior contributes to the improvement in impermeability of the coating, thereby blocking the longitudinal penetration of corrosive medium in the coating, prolonging the coating service and reducing corrosion rate of metal substrate. However, EP-3 shows decreased $|Z|_{0.01}$ value and relatively higher descent rate compared with EP-1, which may be caused by pores presence and

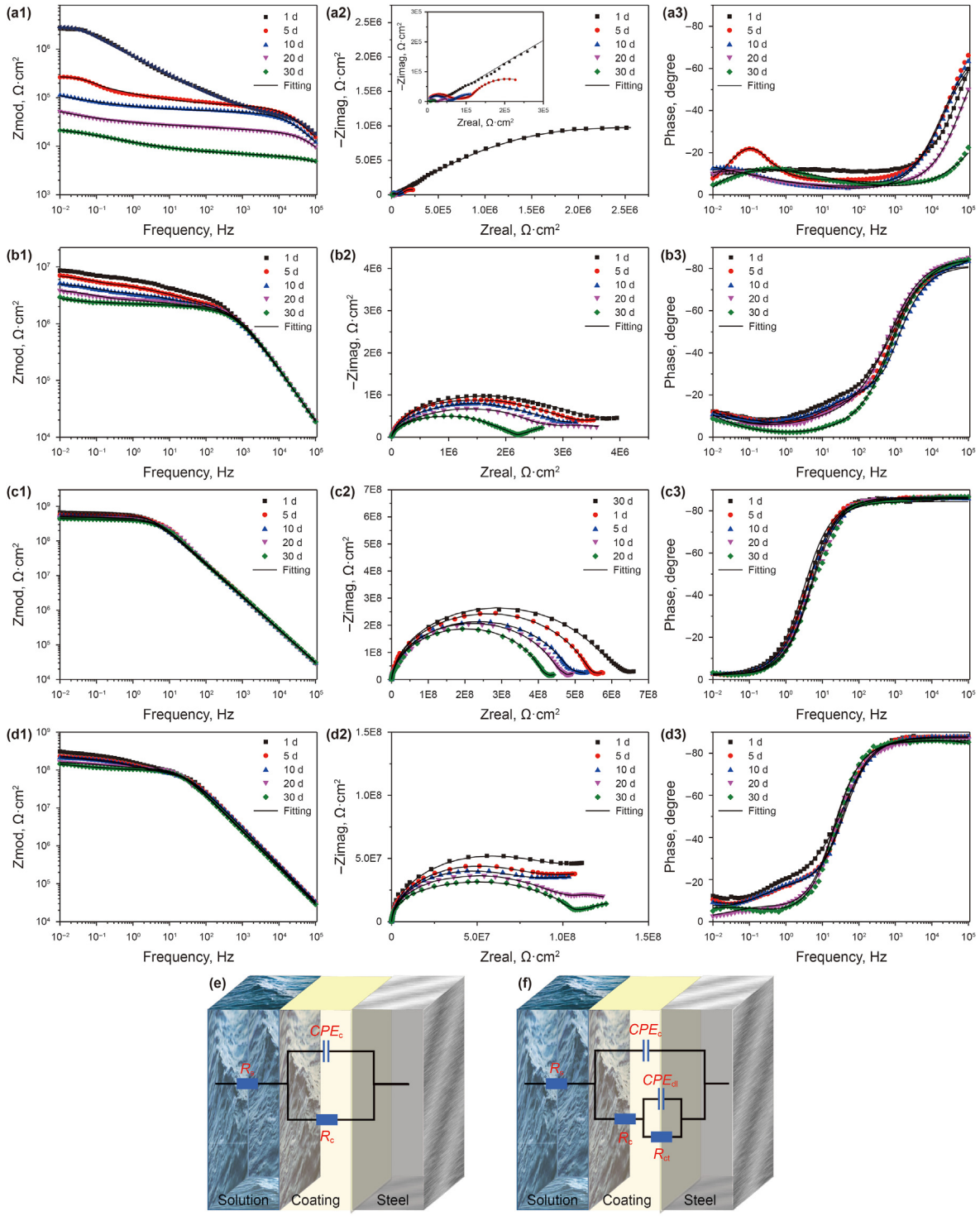

Fig. 7. EIS plots of (**a1**–**a3**) EP-0, (**b1**–**b3**) EP-0.5, (**c1**–**c3**) EP-1, (**d1**–**d3**) EP-3 in oxygen-saturated 3.5 wt% NaCl for different immersion time, equivalent circuits before (**e**) and after failure (**f**).

aggregation of high content Fe–N–C. Besides, the corrosion resistance of coating can also be reflected by the radius of impedance arc in Nyquist plots. Generally, larger radius means a better corrosion resistance of the coating. Similar to the Bode plots, gradual decrease in corrosion resistance of all coatings is found with the immersion time. Among them, EP-1 exhibits the slowest decline rate compared with the other coatings. To further demonstrate the contribution of introduced Fe–N–C to the anticorrosion performance of the coating, N–C with lower catalytic capacity is introduced into the coating as a control. As shown in Fig. 8, the resistance of the EP-NC decreases gradually with the increase of immersion time from 1.03×10^8 to 8.44×10^6 Ω cm^2, which indicated that the coating could not provide effective long-term protection due the lack of sufficient catalytic capacity to consume diffused oxygen. The SEM image and EDS of the carbon steel after removal of the coating further reflect the protection effect, i.e., the steel under EP-NC

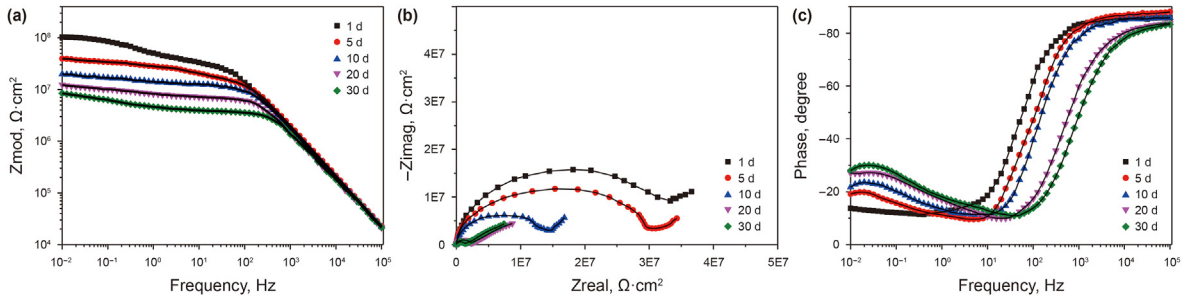

Fig. 8. EIS plots of EP-NC in oxygen saturated 3.5 wt% NaCl for different immersion time.

coating exhibits better protection than EP-0 but ability inferior to EP-1. Such comparison analysis among pure epoxy, N–C and Fe–N–C doped coatings more fully reflects the contribution of introduced Fe–N–C catalysts to the anticorrosion performance of the coating.

Apart from $|Z|_{0.01}$, the failure process of coating can also be vividly revealed by the time constants in Phase plots. Specifically, the time constants at high frequencies and low frequencies reflect the capacitance characteristics of coating and the corrosion response of metal substrate, respectively. As the service time increases, the corrosive media gradually penetrate into the coating, resulting in increase of coating capacitance and decrease of coating resistance. However, coating still can act as effective barrier to protect metal substrate from corrosion as long as the corrosive media don't contact the substrate. At this point, there is only one time constant in the Phase plots. If the corrosive media penetrate into the interface between coating and metal substrate, metal corrosion occurs and simultaneously break the combination of coating and metal. Two time constants will be appeared in the Phase plots. As shown in the Phase diagram of EP-0 (Fig. 7), two time constants are observed after 5 days of immersion, which means that the corrosive media have penetrated through coating and reached metal substrate. The EP-0 lost its protective effect after that and the corrosion rate of metal substrate is prominently accelerated. In contrast, only one time constant can be found for the Fe–N–C doped composite coatings during the whole immersion duration. This suggests that the introduction of Fe–N–C can help the epoxy coating obstruct the penetration of corrosive media, making them cannot contact the metal substrate after long-term immersion.

For deep understanding of the failure process of coating and electrochemical reaction at the interface between the coating and metal substrate, EIS fitting was performed according to the equivalent circuit models (Fig. 7), which are selected in line with the penetration degree of corrosive media in coatings and corrosion evolution of metal substrate as reflected in the Nyquist plots. The equivalent circuit model is in Fig. 7(e) before the corrosive media reach the metal substrate, as shown in Fig. 7(f) after that. The parameters R_s, R_c and R_{ct} are resistance of the solution, resistance of the coating and the charge transfer resistance, respectively. C_c and C_{dl} correspond to capacitance of the coating and double-layer capacitance, respectively. The fitting results are shown in Table S2 and Fig. S8, which are well in agreement with the experimental data. Among the fitting parameters, R_c is the most direct parameter reflecting the protective effect of coating. The higher the R_c value, the better the corrosion protection performance. Moreover, the coating structure and composition are the determining factors for the R_c of the coating, i.e. only coatings with a complete structure have higher R_c values. As shown in Fig. S8(a), coatings with Fe–N–C always keep relative stable R_c value without apparent decline compared with the EP-0. This indicates that the introduced Fe–N–C could assist coating to resist the persistent attack of corrosive media while keeping the coating structure and morphology stable and providing long-term excellent corrosion protection for metals substrate. By comparison, the EP-0 suffers from gradual degradation and loses its protection effect for metals substrate under the attack of corrosive media (O_2, etc.). We attribute this performance difference to active anticorrosion function of epoxy coating brought by introduced Fe–N–C. Compared with traditional single passive barrier, the Fe–N–C doped coating could spontaneously block, adsorb, and deplete the diffused corrosive species (O_2), thus inhibiting metal corrosion as far as possible on the basis of previous barrier function. The coating capacitance (C_c), related to corrosive media uptake can also reveal the failure mechanism of coating. Fig. S8(c) shows the C_c value of coating samples, values of all coatings increase with the immersion time while Fe–N–C doped coating exhibits smaller increment. This shows that less corrosive media diffuses into Fe–N–C doped coatings due to the closure of diffusion channels and the depletion of diffused O_2 by doped Fe–N–C, which could still provide excellent anticorrosion for metal substrate. However, EP-0 with single barrier function suffers from degradation due to gradual penetration of corrosive media. The results for coating capacitance and coating resistance confirm that this nanocatalytic anticorrosion concept could address the limitation of single passive barrier of polymer coating.

The C_{dl} that accurately reflects the contact area of carbon steel with corrosive medium can reveal the blocking effect of coating against corrosive media. According to the analysis from Fig. S8(d), the EP-0 possesses relatively higher C_{dl} value, indicating that more corrosive media penetrate through coating and reach the coating/metal interface. This induces metal corrosion and coating delamination. For Fe–N–C doped coatings, only slight corrosion occurs due to the blocking and depleting effect for corrosive media. Furthermore, R_{ct} is also adopt to reflect the protection effect of coating because it stands for the propensity for electrochemical reaction to occur at the interface. Generally, the higher the R_{ct} value, the slower corrosion reaction and the better coating protection. It can be found that after introduction of Fe–N–C, the R_{ct} value exhibits significant improvement, which means that the metal corrosion is sufficiently suppressed. Based on the EIS analysis, it can be concluded that the introduced Fe–N–C confers active long-term corrosion protection to the coating through synergistic corrosive media blocking and depletion effect.

In addition to electrochemical characterization, the anticorrosion performance of Fe–N–C doped coatings were also confirmed by corrosion and products studies. The corrosion morphology and products of carbon steel were analyzed after careful removal of the coating, as shown in Fig. 9. It can be found that the surface of steel coated by pure epoxy is uneven and massive corrosion products accumulate. According to the EDS analysis, the corrosion products

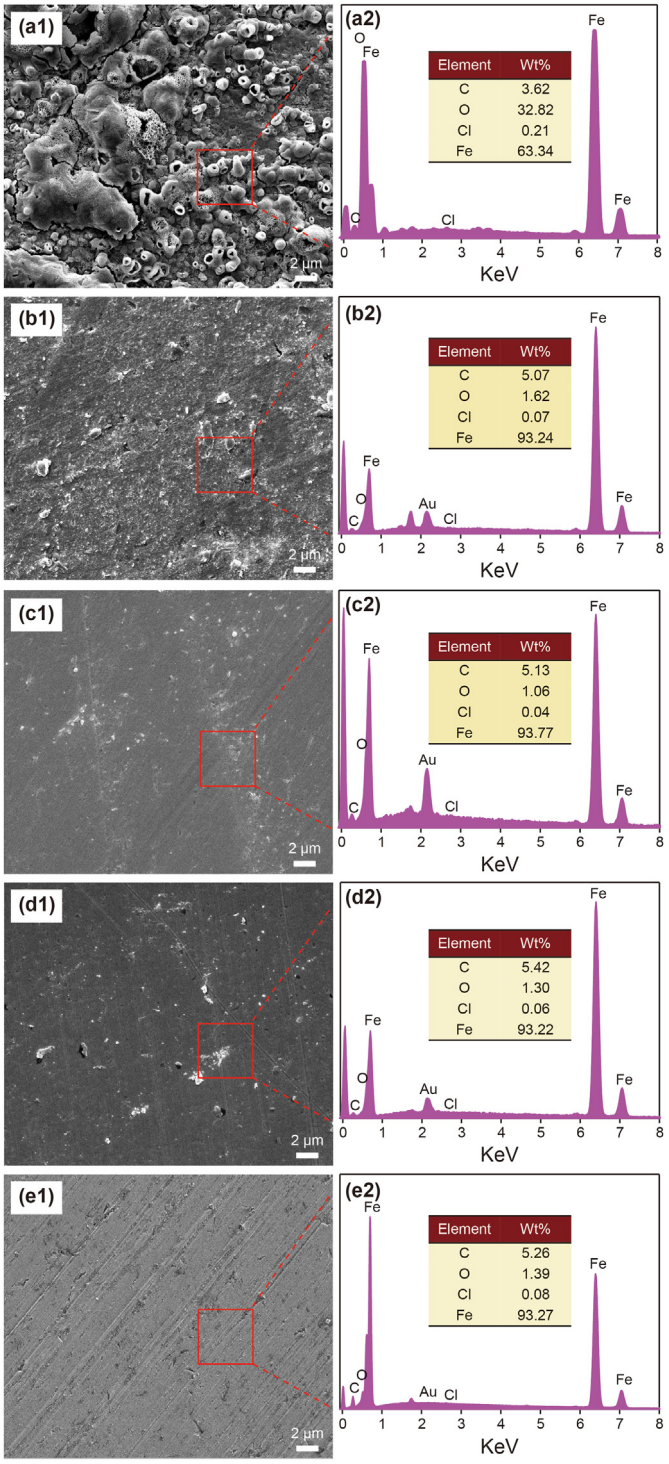

Fig. 9. SEM images and EDS of (**a1**, **a2**) EP-0, (**b1**, **b2**) EP-0.5, (**c1**, **c2**) EP-1, (**d1**, **d2**) EP-3 and (**e1**, **e2**) EP-NC coated carbon steel immersed in oxygen-saturated 3.5 wt% NaCl after 30 days.

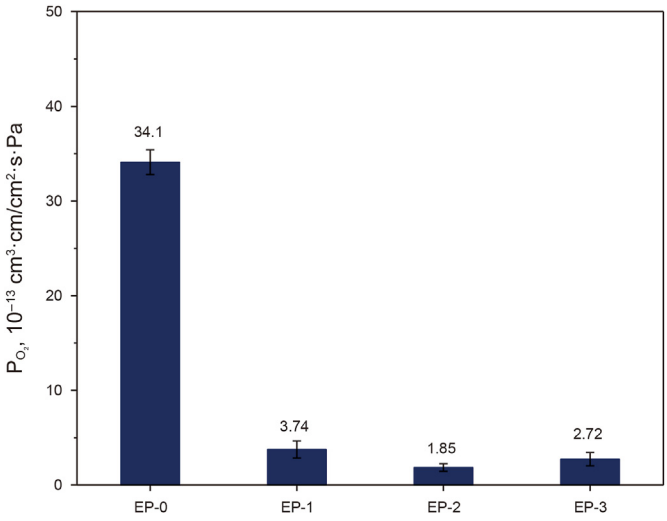

Fig. 10. Oxygen permeability coefficient of different coating samples.

are mainly composed of oxygen, chlorine and iron elements. By contrast, only slight corrosion occurs on the steel protected by Fe–N–C doped coatings, with much less corrosion products presented. This indicates that the anticorrosion performance of coating is effectively enhanced after the introduction of Fe–N–C catalyst, resulting from their uniform distribution and significantly blocking and depletion of corrosive media in coating. Among which, the EP-1 shows the optimal corrosion resistance and the steel beneath has the smoothest surface. Moreover, the improved anticorrosion performance by introduced catalyst is also revealed by the composition analysis of corrosion products. The comparison of Fig. 9(a2) to (e2) shows that the corrosion products on EP-0 coated steel possesses the highest oxygen content, while the corrosion products on steel coated by Fe–N–C doped coatings contain relatively lower oxygen element, with EP-1 coated steel having the lowest level of corrosion products. This composition difference confirms that the addition of evenly distributed Fe–N–C catalyst can effectively deplete the oxygen corrosive medium, resulting in only very little oxygen being able to penetrate to the steel surface and giving the coating improved anticorrosion performance. Despite the better anticorrosion effect compared with EP-0, the anticorrosion effect exceeding EP-1 is not achieved after loading excessive catalyst into coating. We speculate that the higher content of catalyst is difficult to disperse uniformly in the coating, which will lead to aggregation of catalyst, emergence of pores for corrosive media transportation and decrease in the anticorrosion performance of the coating. The conclusions obtained are well consistent with the results of electrochemical analysis. Furthermore, the AFM images of carbon steel after removal of corrosion products were also obtained to intuitively demonstrate the improved corrosion resistance of the coating. As shown in Fig. S9, the steel surfaces become smoother after the introduction of Fe–N–C catalyst into coatings, with the roughest surface of steel under EP-0 and the smoothest surface of steel under EP-1, which implies serious and slight corrosion of steel, respectively. The combination of electrochemical and surface analysis results demonstrates that the nanocatalytic anticorrosion concept through addition of Fe–N–C catalyst can indeed achieve active regulation of corrosive media and enhance the protection effect of polymer coating.

In addition to the oxygen consumption verification, the barrier performance of composite coatings was also evaluated via the oxygen permeability test to gain the insight of improved anticorrosion performance. Fig. 10 shows the oxygen permeability coefficient of all the coatings. The Fe–N–C doped coatings exhibits smaller coefficient from 1.85×10^{-13} to 3.74×10^{-13} $cm^3 \cdot cm/cm^2 \cdot s \cdot Pa$ compared to pure epoxy, indicating that much less oxygen could penetrate through the coating after introduction of Fe–N–C catalyst, that is, the introduction of Fe–N–C improves the shielding effect of the coating and blocks the penetration of oxygen. The specific corrosion protection process of Fe–N–C doped coating is

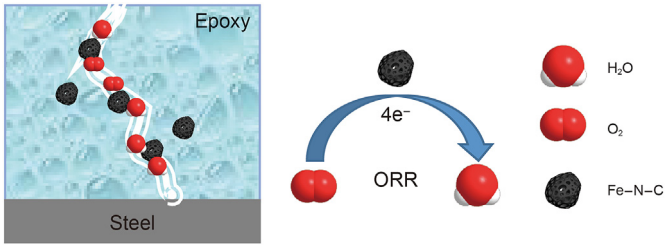

Scheme 2. Proposed nanocatalytic anticorrosion mechanism.

illustrated in Scheme 2. For pure epoxy coating, the pores and cracks formed during the curing process will provide unobstructed diffusion channels for corrosive media, leading to their fast penetration to the steel surface and subsequent rapid and serious corrosion. For coating doped with Fe–N–C catalyst, the uniformly distributed Fe–N–C filler firstly contributes to the improvement of coating compactness according to the dispersion characterization results of Fe–N–C catalyst in the coating. Then, partial diffused oxygen will be preferentially trapped and directly reduced by added Fe–N–C. This synergistic blocking and depleting effect actively slow down the penetration of corrosive media and metal corrosion as much as possible. Based on the above verification, the introduced Fe–N–C catalyst does effectively demonstrate the feasibility of the nanocatalytic anticorrosion concept.

4. Conclusions

In summary, one feasible nanocatalytic anticorrosion concept based on oxygen depletion by catalyst is proposed. Firstly, single-atom Fe–N–C catalyst was prepared through controlled hydrolysis and polymerization of pre-coordinated iron/organosilane followed by direct carbonization. The obtained Fe–N–C with isolated Fe–N_4 centers exhibits excellent oxygen reduction activity (E_{onset} of 1.02 V and $E_{1/2}$ of 0.89 V) due to the molecular and spatial confinement. After introduced into epoxy coating, Fe–N–C catalyst distributes uniformly, occupying the holes and cracks of coating, resulting in a significant reduction in the permeability of corrosive media through the coating. Meanwhile, the doped Fe–N–C can proactively trap the diffused oxygen and consume them. Under this active synergistic mechanism of blocking and depleting, the durable anticorrosion performance of the coating is guaranteed. The Fe–N–C doped coating does not show obvious decline in the corrosion resistance, accompany with no apparent corrosion of steel under protection after immersion test. This new protection mechanism through such mediation of corrosive media is expected to further promote the innovative development and practical application of smart anticorrosion coatings in petroleum science.

Declaration of competing interest

The authors declare the following financial interests/personal relationships which may be considered as potential competing interests: Songqing Hu reports financial support was provided by National Natural Science Foundation of China.

Acknowledgement

This research was financially supported by the “National Natural Science Foundation of China” (52304072), “Funded by Shandong Postdoctora1 Science Foundation” (SDBX2023019), the “Fundamental Research Funds for the Central Universities” (23CX06022A), the “Applied Research Project of Qingdao Postdoctoral Researchers” (QDBSH20230202010).

Appendix A. Supplementary data

Supplementary data to this article can be found online at https://doi.org/10.1016/j.petsci.2023.05.019.

References

Abdullayev, E., Abbasov, V., Tursunbayeva, A., et al., 2013. Self-healing coatings based on halloysite clay polymer composites for protection of copper alloys. ACS Appl. Mater. Interfaces. 5 (10), 4464–4471. https://doi.org/10.1021/am400936m.

Bahremand, F., Shahrabi, T., Ramezanzadeh, B., 2021. Epoxy coating anti-corrosion properties enhancement via the steel surface treatment by nanostructured samarium oxide-poly-dopamine film. J. Hazard Mater. 403, 123722. https://doi.org/10.1016/j.jhazmat.2020.123722.

Borisova, D., Möhwald, H., Shchukin, D.G., 2011. Mesoporous silica nanoparticles for active corrosion protection. ACS Nano 5 (3), 1939–1946. https://doi.org/10.1021/nn102871v.

Borisova, D., Möhwald, H., Shchukin, D.G., 2012. Influence of embedded nanocontainers on the efficiency of active anticorrosive coatings for aluminum alloys part i: influence of nanocontainer concentration. ACS Appl. Mater. Interfaces. 4 (6), 2931–2939. https://doi.org/10.1021/am300266t.

Borisova, D., Akçakayıran, D., Schenderlein, M., et al., 2013. Nanocontainer-based anticorrosive coatings: effect of the container size on the self-healing performance. Adv. Funct. Mater. 23 (30), 3799–3812. https://doi.org/10.1002/adfm.201203715.

Fu, J., Chen, T., Wang, M., et al., 2013. Acid and alkaline dual stimuli-responsive mechanized hollow mesoporous silica nanoparticles as smart nanocontainers for intelligent anticorrosion coatings. ACS Nano 7 (12), 11397–11408. https://doi.org/10.1021/nn4053233.

He, Y., Dobryden, I., Pan, J., et al., 2018. Nano-scale mechanical and wear properties of a waterborne hydroxyacrylic-melamine anti-corrosion coating. Appl. Surf. Sci. 457, 548–558. https://doi.org/10.1016/j.apsusc.2018.06.284.

Jin, H., Zhao, X., Liang, L., et al., 2021. Sulfate ions induced concave porous S-N co-doped carbon confined FeC_x nanoclusters with Fe-N_4 sites for efficient oxygen reduction in alkaline and acid media. Small 17 (29), 2101001. https://doi.org/10.1002/smll.202101001.

Kim, H., Kim, S., Park, C., et al., 2010. Glutathione-induced intracellular release of guests from mesoporous silica nanocontainers with cyclodextrin gatekeepers. Adv. Mater. 22 (38), 4280–4283. https://doi.org/10.1002/adma.201001417.

Lai, J., Shah, B.P., Garfunkel, E., et al., 2013. Versatile fluorescence resonance energy transfer-based mesoporous silica nanoparticles for real-time monitoring of drug release. ACS Nano 7 (3), 2741–2750. https://doi.org/10.1021/nn400199t.

Li, G.L., Zheng, Z., Möhwald, H., et al., 2013. Silica/polymer double-walled hybrid nanotubes: synthesis and application as stimuli-responsive nanocontainers in self-healing coatings. ACS Nano 7 (3), 2470–2478. https://doi.org/10.1021/nn305814q.

Li, J.C., Maurya, S., Kim, Y.S., et al., 2020. Stabilizing single-atom iron electrocatalysts for oxygen reduction via ceria confining and trapping. ACS Catal. 10 (4), 2452–2458. https://doi.org/10.1021/acscatal.9b04621.

Liu, C., Zhao, H., Hou, P., et al., 2018. Efficient graphene/cyclodextrin-based nanocontainer: synthesis and host–guest inclusion for self-healing anticorrosion application. ACS Appl. Mater. Interfaces. 10 (42), 36229–36239. https://doi.org/10.1021/acsami.8b11108.

Liu, C., Qian, B., Hou, P., et al., 2021. Stimulus responsive zeolitic imidazolate framework to achieve corrosion sensing and active protecting in polymeric coatings. ACS Appl. Mater. Interfaces. 13 (3), 4429–4441. https://doi.org/10.1021/acsami.0c22642.

Luo, E., Chu, Y., Liu, J., et al., 2021. Pyrolyzed M–N_x catalysts for oxygen reduction reaction: progress and prospects. Energy Environ. Sci. 14 (4), 2158–2185. https://doi.org/10.1039/D1EE00142F.

Machuca, L.L., Jeffrey, R., Bailey, S.I., et al., 2014. Filtration–uv irradiation as an option for mitigating the risk of microbiologically influenced corrosion of subsea construction alloys in seawater. Corrosion Sci. 79, 89–99. https://doi.org/10.1016/j.corsci.2013.10.030.

Mao, M., Jiang, L., Wu, L., et al., 2015. The structure control of ZnS/graphene composites and their excellent properties for lithium-ion batteries. J. Mater. Chem. 3 (25), 13384–13389. https://doi.org/10.1039/C5TA01501D.

Najmi, P., Keshmiri, N., Ramezanzadeh, M., et al., 2021. Synthesis and application of Zn-doped polyaniline modified multi-walled carbon nanotubes as stimuli-responsive nanocarrier in the epoxy matrix for achieving excellent barrier-self-healing corrosion protection potency. Chem. Eng. J. 412, 128637. https://doi.org/10.1016/j.cej.2021.128637.

Ning, F., Tan, J., Zhang, Z., et al., 2021. Effects of thiosulfate and dissolved oxygen on crevice corrosion of alloy 690 in high-temperature chloride solution. J. Mater. Sci. Technol. 66, 163–176. https://doi.org/10.1016/j.jmst.2020.05.074.

Qian, H., Xu, D., Du, C., et al., 2017. Dual-action smart coatings with a self-healing superhydrophobic surface and anti-corrosion properties. J. Mater. Chem. 5 (5), 2355–2364. https://doi.org/10.1039/C6TA10903A.

Qian, B., Zheng, Z., Michailids, M., et al., 2019. Mussel-inspired self-healing coatings

based on polydopamine-coated nanocontainers for corrosion protection. ACS Appl. Mater. Interfaces 11 (10), 10283–10291. https://doi.org/10.1021/acsami.8b21197.
Qiu, S., Li, W., Zheng, W., et al., 2017. Synergistic effect of polypyrrole-intercalated graphene for enhanced corrosion protection of aqueous coating in 3.5% NaCl solution. ACS Appl. Mater. Interfaces. 9 (39), 34294–34304. https://doi.org/10.1021/acsami.7b08325.
Qu, Y., Wang, L., Li, Z., et al., 2019. Ambient synthesis of single-atom catalysts from bulk metal via trapping of atoms by surface dangling bonds. Adv. Mater. 31 (44), 1904496. https://doi.org/10.1002/adma.201904496.
Shchukin, D.G., Möhwald, H., 2007. Self-repairing coatings containing active nanoreservoirs. Small 3 (6), 926–943. https://doi.org/10.1002/smll.200700064.
Shen, J., Liu, H., Mu, C., et al., 2017. Multi-step encapsulation of chemotherapy and gene silencing agents in functionalized mesoporous silica nanoparticles. Nanoscale 9 (16), 5329–5341. https://doi.org/10.1039/C7NR00377C.
Skorb, E.V., Andreeva, D.V., 2013. Layer-by-layer approaches for formation of smart self-healing materials. Polym. Chem. 4 (18), 4834–4845. https://doi.org/10.1039/C3PY00088E.
Suedile, F., Robert, F., Roos, C., et al., 2014. Corrosion inhibition of zinc by Mansoa alliacea plant extract in sodium chloride media: extraction, characterization and electrochemical studies. Electrochim. Acta. 133, 631–638. https://doi.org/10.1016/j.electacta.2013.12.070.
Sun, W., Wang, L., Wu, T., et al., 2015. Inhibiting the corrosion-promotion activity of graphene. Chem. Mater. 27 (7), 2367–2373. https://doi.org/10.1021/cm5043099.
Sun, Y., Fu, D., Zhu, Y., et al., 2022. A novel anti-oxygen composite coating and its corrosion resistance mechanism. Corrosion Sci. 201, 110298. https://doi.org/10.1016/j.corsci.2022.110298.
Tavandashti, N.P., Ghorbani, M., Shojaei, A., et al., 2016. Inhibitor-loaded conducting polymer capsules for active corrosion protection of coating defects. Corrosion Sci. 112, 138–149. https://doi.org/10.1016/j.corsci.2016.07.003.
Tian, Y., Guo, R., Jiao, Y., et al., 2016. Redox stimuli-responsive hollow mesoporous silica nanocarriers for targeted drug delivery in cancer therapy. Nanoscale Horizons 1 (6), 480–487. https://doi.org/10.1039/C6NH00139D.
Tian, G., Zhang, M., Zhao, Y., et al., 2019. High corrosion protection performance of a novel nonfluorinated biomimetic superhydrophobic Zn-Fe coating with echinopsis multiplex-like structure. ACS Appl. Mater. Interfaces 11 (41), 38205–38217. https://doi.org/10.1021/acsami.9b15088.
Wang, C., Li, Z., Cao, D., et al., 2012. Stimulated release of size-selected cargos in succession from mesoporous silica nanoparticles. Angew. Chem. Int. Ed. 51 (22), 5460–5465. https://doi.org/10.1002/anie.201107960.
Wang, X., Li, C., Zhang, M., et al., 2022. A novel waterborne epoxy coating with anti-corrosion performance under harsh oxygen environment. Chem. Eng. J. 430, 133156. https://doi.org/10.1016/j.cej.2021.133156.
White, S.R., Sottos, N.R., Geubelle, P.H., et al., 2001. Autonomic healing of polymer composites. Nature 409 (6822), 794–797. https://doi.org/10.1038/35057232.
Ye, Y., Liu, Z., Liu, W., et al., 2018. Superhydrophobic oligoaniline-containing electroactive silica coating as pre-process coating for corrosion protection of carbon steel. Chem. Eng. J. 348, 940–951. https://doi.org/10.1016/j.cej.2018.02.053.
Ye, Y., Chen, H., Zou, Y., et al., 2020. Corrosion protective mechanism of smart graphene-based self-healing coating on carbon steel. Corrosion Sci. 174, 108825. https://doi.org/10.1016/j.corsci.2020.108825.
Yu, Z., Di, H., Ma, Y., et al., 2015. Fabrication of graphene oxide–alumina hybrids to reinforce the anti-corrosion performance of composite epoxy coatings. Appl. Surf. Sci. 351, 986–996. https://doi.org/10.1016/j.apsusc.2015.06.026.
Zeng, H., Yang, Y., Zeng, M., et al., 2021. Effect of dissolved oxygen on electrochemical corrosion behavior of 2205 duplex stainless steel in hot concentrated seawater. J. Mater. Sci. Technol. 66, 177–185. https://doi.org/10.1016/j.jmst.2020.06.030.
Zhao, H., Yue, Y., Guo, L., et al., 2016. Cloning nacre's 3d interlocking skeleton in engineering composites to achieve exceptional mechanical properties. Adv. Mater. 28 (25), 5099–5105. https://doi.org/10.1002/adma.201600839.
Zhao, Y., Jiang, F., Chen, Y.Q., et al., 2020. Coatings embedded with go/mofs nanocontainers having both active and passive protecting properties. Corrosion Sci. 168, 108563. https://doi.org/10.1016/j.corsci.2020.108563.
Zheludkevich, M.L., Shchukin, D.G., Yasakau, K.A., et al., 2007. Anticorrosion coatings with self-healing effect based on nanocontainers impregnated with corrosion inhibitor. Chem. Mater. 19 (3), 402–411. https://doi.org/10.1021/cm062066k.
Zheng, Z., Huang, X., Schenderlein, M., et al., 2013. Self-healing and antifouling multifunctional coatings based on pH and sulfide ion sensitive nanocontainers. Adv. Funct. Mater. 23 (26), 3307–3314. https://doi.org/10.1002/adfm.201203180.
Zhou, Y., Yu, Y., Ma, D., et al., 2020. Atomic Fe dispersed hierarchical mesoporous Fe–N–C nanostructures for an efficient oxygen reduction reaction. ACS Catal. 11 (1), 74–81. https://doi.org/10.1021/acscatal.0c03496.